Investigation of structure-spectroscopy-function relationship of two-dimensional J-aggregates of tetrachlorobenzimidazolorcarbocyanine preferentially oriented in poly-vinly-alcohol thin films

Chemical Physics 355 (2009) 73–80

Contents lists available at ScienceDirect

Chemical Physics

journal homepage: www.elsevier.com/locate/chemphys

Investigation of structure–spectroscopy–function relationship of two-dimensional J-aggregates of tetrachlorobenzimidazolocarbocyanine preferentially oriented in poly-vinyl-alcohol thin films

Demet Gülen [a,*], Onur Atasoylu [b], Serdar Özçelik [b,*]

[a] Physics Department, Middle East Technical University, 06531 Ankara, Turkey
[b] Chemistry Department, İzmir Institute of Technology, Urla-35430, İzmir, Turkey

ARTICLE INFO

Article history:
Received 28 December 2007
Accepted 6 November 2008
Available online 12 November 2008

Keywords:
J-aggregates
Frenkel exciton
Phonon-assisted exciton relaxation
Davydov splitting
Polarized UV–Vis absorption
Vertical spin coating
Cyanines

ABSTRACT

The structure–spectroscopy–function relationship of 1,1′,3,3′-tetraethyl-5,5′,6,6′-tetrachlorobenzimidazolocarbocyanine (TTBC) aggregates is studied using a combination of experimental and theoretical techniques. The aggregates are macroscopically aligned in poly-vinyl-alcohol thin films by vertical spin coating. Angular dependence of the UV–Vis spectra is measured at eleven different orientations between the electric field polarization and the macroscopic alignment axis. The aggregates are characterized by a pair of Davydov split bands with opposite polarization behaviors: an H-band (505 nm) and a J-band (594 nm) polarized respectively, close to being parallel and perpendicular to the alignment axis. Spectral response is interpreted via simulations within the Frenkel exciton formalism. TTBC aggregates are shown to assume very similar internal molecular packing (herringbone) and dynamics of excited states (phonon-assisted intraband and interband relaxations) in ionic aqueous solution and in thin films. The general conclusions on the structure–spectroscopy–function relationship are expected to hold for other cyanine aggregates with the same generic spectral features.

1. Introduction

Cyanines are organic dye molecules which can be spontaneously self-assembled into ordered molecular aggregates as discovered by Jelley [1] and Scheibe [2]. Self-assembled cyanine aggregates can exhibit interesting collective linear and nonlinear optical/excitonic properties [3].

Successful utilization of cyanine aggregates in photographic industry has a long history [4]. Cyanine aggregates continue to attract attention owing to their wide range of current applications. One of the well-established current application is exploitation of spectroscopic properties of TTBC (1,1′,3,3′-tetraethyl-5,5′,6,6′-tetrachlorobenzimidazolocarbocyanine) as an imaging probe in molecular cell biology [5,6]. They also show potential as artificial light-harvesting complexes [7], electronic energy transport wires [8], and as promising materials for applications in ultrafast optical switching [9].

Reaching a control on the mesoscopic morphology and internal molecular arrangement of cyanine aggregates is an important step for realization of devices with tailor-made optical properties. The lowest energy band/the J-band of the cyanine aggregates is a narrow red-shifted superradiant state which is strongly polarized. It is, therefore, of particular importance for potential device applications to characterize thin films in which the aggregates are aligned preferentially. Of the techniques, vertical spin coating, in which the centrifugal force is used to align the aggregates, is well-known to produce thin films consisting of preferentially oriented aggregates [10,11]. It is suggested that this technique produces films durable at room temperature in which the preferential alignment of the long J-aggregates is in the film growth direction [10,11]. Detection of the incident polarization dependence of spectral response of the aggregates with a well-defined macroscopic alignment direction can be very advantageous for characterizing the aggregates.

A good understanding of the dependence of exciton structure and dynamics on model spatial structures is emerging [12–20]. Further testing of the mechanisms is however hampered by the insufficiency of knowledge in internal molecular arrangements since the current techniques [21] do not easily allow structural determination at atomic resolution. Therefore, elucidation of the characteristics of cyanine aggregates within a structure–spectroscopy–function relationship is often bound to an access from spectroscopic data. On the other hand, even if a well-resolved structural model is available, a comprehensive understanding of the structure–spectroscopy–function relationship still requires

* Corresponding authors. Tel.: +90 312 210 5060; fax: +90 312 210 5099 (D. Gülen); tel.: +90 232 750 7557; fax: +90 232 750 7509 (S. Özçelik).
E-mail addresses: dgul@metu.edu.tr (D. Gülen), serdarozcelik@iyte.edu.tr (S. Özçelik).

0301-0104/$ - see front matter © 2008 Elsevier B.V. All rights reserved.
doi:10.1016/j.chemphys.2008.11.005

extensive modeling of excitonic states and their dynamics, as for example experienced in the case of photosynthetic light-harvesting and reaction center complexes [7,22–25]. In the case of cyanine aggregates, the spectroscopic data have more often been interpreted on the basis of simulations that are constrained to evaluating the structure and steady-state (static) aspects of the spectral response [12,13]. There is an accelerated interest and progress in understanding the functional/dynamical aspects in a quantitative context along with the electronic excited state structure [14–20].

To this end we have carried out a comprehensive investigation of the structure–spectroscopy–function relationship of the TTBC aggregates in PVA (poly-vinyl-alcohol) thin films by a combination of experimental and theoretical techniques. Polarization characteristics of the UV–Vis absorption of thin films prepared by vertical spin coating have been assessed experimentally at several different directions between the polarization of electric field and the macroscopic alignment axis. The experimental results have been quantified by employing simulations obtained in the Frenkel exciton formalism [26,27] augmented by diagonal energetic disorder [28] and exciton–phonon coupling [29] in order to address the excitation dynamics in addition to the static properties of the aggregate excited states.

2. Experimental methods

TTBC (Hayashibara, Japan) was used without further purification. PVA (Aldrich, USA) was used as received. Thin films of aggregates dispersed in PVA films were prepared by the vertical spin coating method [10,11]. The spectra were recorded by an HP Agilent 8543 diode array spectrophotometer (resolution of 0.5 nm) at room temperature. The electric field polarization direction of the excitation was adjusted by inserting a linear glass polarizer (100:1) between the slit of the spectrophotometer and the sample. The film was placed on a rotating stage. The growth axis of the film and the electric field polarization direction were adjusted parallel to the 0–180° axis of a rotating stage. The stage was rotated (around an axis perpendicular to the substrate surface) until absorbance around 500 nm has reached to its maximum. The direction satisfying this condition will be referred as the macroscopic alignment axis. The angle between the electric field polarization and the macroscopic alignment axis was changed by rotating the stage further in the same direction at 10–20° steps. Angular dependence of the UV–Vis spectra was measured at eleven different orientations between the electric field and the macroscopic alignment axis.

The geometry illustrated in Fig. 1 sets up the connection with the measurements. The electric field vector ($\vec{E}$) is parallel to the substrate surface and is polarized along the laboratory axis. The rotation of the substrate controls the angle (θ) between the macroscopic alignment axis and $\vec{E}$. γ defines the orientation of the aggregate axis with respect to the macroscopic alignment axis. That is, $\theta' = \theta - \gamma$ is the angle between $\vec{E}$ and the aggregate axis. The quantity measured is the absorption strength (absorbance) parallel to the electric field at each θ. $\vec{M}_v$ is the dipole moment associated with the vth excitonic transition. It has a definite orientation in the aggregate. β_v defines its polarization with respect to the aggregate axis. For the vth excitonic transition, at polarization θ, the normalized absorption strengths parallel and perpendicular to the electric field vector are respectively given by [30]

$$A_{\mathrm{II},v}/A_{\mathrm{iso},v} = 1 + 2P_2(\cos\theta') \cdot P_2(\cos\beta_v) \quad (1a)$$

and

$$A_{\perp,v}/A_{\mathrm{iso},v} = 1 - P_2(\cos\theta') \cdot P_2(\cos\beta_v). \quad (1b)$$

In Eqs. (1a) and (1b) the isotropic absorption of the vth excitonic transition, $A_{\mathrm{iso},v}$ is defined as $A_{\mathrm{iso},v} = (A_{\mathrm{II},v} + 2A_{\perp,v})/3$ and $P_2(\cos x) = (3\cos^2 x - 1)/2$ is the Legendre polynomial of 2nd order. If the alignment is not complete $P_2(\cos\theta')$ in (1a) and (1b) should be replaced by its value averaged over differently oriented aggregates in the sample. We will assume that the alignment is close to being complete for simplicity. For a transition polarized along the aggregate axis ($\beta_v = 0^o$) the maximum value of $A_{\mathrm{II},v}/A_{\mathrm{iso},v}$ is equal to 3 and for a transition polarized perpendicular to the aggregate axis ($\beta_v = 90^o$) it is equal to 1.5. This ½ reduction is caused by the fact that although all transition dipole moments are perfectly aligned perpendicular to the aggregate axis, they still can rotate freely in the plane perpendicular to this axis. The symmetry in absorbance of a given transition should pertain for θ and $(180^o - (\theta - 2\gamma))$ as also exhibited in Fig. 1.

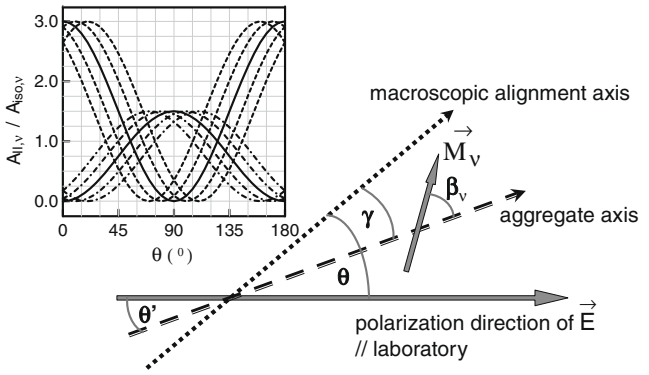

Fig. 1. The geometry that sets up the connection with the measurements. $\vec{M}_v$ stands for the dipole moment associated with the vth excitonic transition. The insert shows the polarization direction dependence of $A_{\mathrm{II},v}/A_{\mathrm{iso},v}$ in this geometry. $\beta_v = 90°$ (the lower set of curves), $\beta_v = 0°$ (the upper set of curves), $\gamma = 0°$ (solid) and $\gamma = -20°$, $-10°$, $10°$, and $20°$, from left to right.

3. Results, analysis and discussion

3.1. UV–Vis absorption spectra

Fig. 2a shows the UV–Vis absorption spectra measured at eleven different polarization directions ranging between $\theta = 0°$ and $\theta = 180°$. The spectra between $\theta = 0°$ and 90° are presented in comparison with the spectra between $\theta = 100°$ and 180°.

The absorption spectrum of monomeric TTBC dissolved in methanol, shown in the insert of Fig. 2a, consists of a 0–0 transition which peaks at 514 nm and a vibrational side band which shoulders around 480 nm.

Two major absorption bands are promoted upon aggregation: a narrow red-shifted band peaking at 594 nm (the J-band) and a broad, blue-shifted band pronounced around 505 nm (the H-band). In addition some monomeric contribution, which is clearly distinguished for the $\theta = 60°$–100° spectra, is present.

The two major aggregate bands exhibit opposite polarization dependence as shown in Fig. 2b. The H-band assumes its maximum intensity when the electric field vector, $\vec{E}$, and the macroscopic alignment axis become almost parallel, that is, θ around 0°, and between 160° and 180°. A gradual decrease in the H-band intensity follows the changes in the polarization direction. The H-band intensity is observed to be strongly reduced and to assume its minimum value when the macroscopic alignment axis become almost perpendicular to the electric field vector that is, for θ around 80°. Conversely, the J-band intensity assumes its minimum (maximum) value when the H-band intensity attains its maximum (minimum). Under the proposition that vertical spin coating technique produces films in which the aggregates long axis lies preferentially along the film growth direction [10,11] the data suggests that the H-band is polarized more or less parallel to the aggregate axis

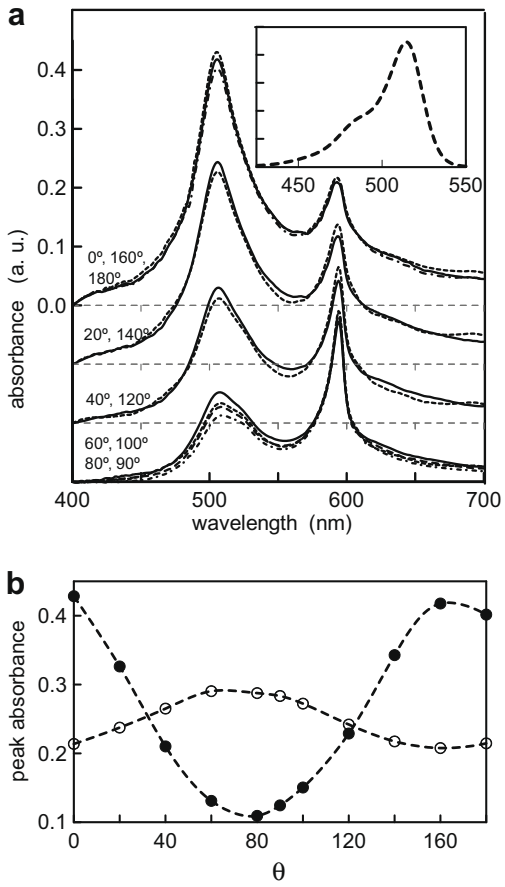

Fig. 2. (a) Polarized absorption spectra for eleven different polarization directions between $\theta = 0°$ and $\theta = 180°$. The spectra are drawn on an apparent scale because concentration of the aggregate molecules is not known accurately. The spectra shifted down by 0.1 are drawn on the same scale as the group of spectra at $\theta = 0°$, 160° and 180°. $\theta = 0°$, 20°, 40°, 60° (dash); $\theta = 80°$ (dash-dot); $\theta = 90°$ (long dash), $\theta = 100°$, 120°, 140°, 160° (solid) and $\theta = 180°$ (dash-dot). The insert shows the monomeric absorption spectrum in methanol in arbitrary units. (b) The θ-dependence of the peak intensities of the H- and J-bands.

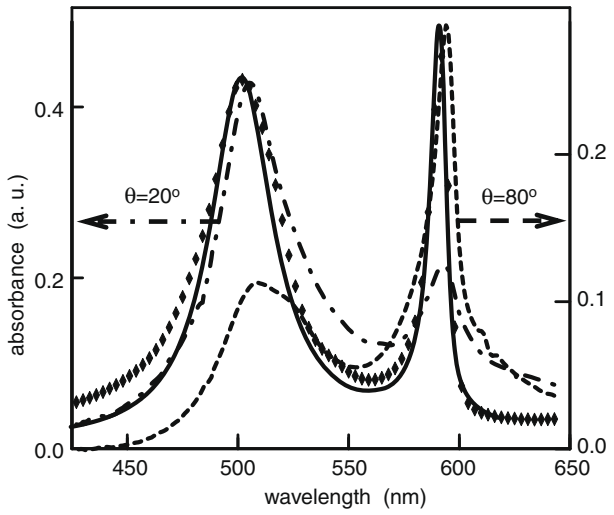

Fig. 3. Comparison of A_{iso} in ionic aqueous solution (0.2 mM TTBC in 0.01 M NaOH solution [16], symbols) with the polarized absorption spectrum for $\theta = 20°$ (dash-dot) and $\theta = 80°$ (dash) and simulation of A_{iso} (solid, taken from Ref. [16]). For the A_{iso} simulation $M_0^2/x^3 = 58.40$ debye^2/nm^3, $M_0^2/y^3 = 339.70$ debye^2/nm^3, $\alpha = 27°$, the dynamical parameters are, $\sigma = 200\ cm^{-1}$, $\hbar S_{intra} = 500\ cm^{-1}$ and $\hbar S_{inter} = 2500\ cm^{-1}$.

and the J-band has a polarization more or less perpendicular to it. The experimentally observed symmetry pertains for polarization directions complementing at about 160°. This observation suggests that the macroscopic alignment of the aggregates is not too far from perfect. The comparison between the theory (insert of Fig. 1) and the experiment (Fig. 2b) indicates that the alignment angle, γ, is around $-10°$.

3.2. Comparison with the isotropic absorption spectra in ionic aqueous solution

We have recently studied the formation of the TTBC aggregates in ionic (NaOH) aqueous solution at room temperature [16]. Fig. 3 compares the polarized absorption spectrum at $\theta = 20°$ and $\theta = 80°$ with the isotropic absorption, A_{iso}, in ionic aqueous solution. The H- and J-band characteristics in solution and in thin film are very similar. The similarities are pertinent to the peak positions and the shapes/widths of the bands. We attribute the differences in the band shape/widths to some spectral heterogeneity and to the enhanced monomeric contribution on the red side of the H-band in the film. It is well-known that the band positions depend to a large extent on the internal molecular arrangement whereas the band shapes/widths are determined basically by the excited state dynamics [14–20]. The immediate conclusion following this comparison is: TTBC aggregates assume very similar internal molecular packing and dynamics of excited states in ionic aqueous solution and in thin films.

We have already carried out a comprehensive analysis of the exciton band structure and the dynamics of the excited states in solution [16]. This analysis was based on the simulations of A_{iso} in the Frenkel exciton formalism [26,27]. A typical simulation shown in Fig. 3 will be detailed later. We first summarize the main results. Strong theoretical evidence was provided on the formation of two-dimensional aggregates assembled in herringbone arrangement on the basis of simulations of isotropic absorption, which were satisfactory in fitting the bandshape and widths in addition to band positions. Accordingly, the H- and J-bands were identified as a Davydov split pair [27] that resulted from the coupling between the two J-aggregate chains. In addition the wide gap between the Davydov split bands was suggested to be bridged by the exciton band(s) of the loosely coupled chains and the monomeric species. The dynamics of the excited states were attributed to disorder-induced phonon-assisted intraband and interband exciton relaxations. The intraband dynamics in both bands were estimated to occur on the same time scale (about a picosecond) and could alone account for the J-band shape. The width and the shape of the H-band were explained by further lifetime shortening of the excitonic states of H-band through the interband processes. Very fast interband dynamics (≈50 fs) has been accounted by, either direct relaxation from the H- to J-band or relaxation via the gap states and energy transfer to monomeric species.

The data presented in Fig. 2 are in qualitative accord with what is expected of the polarization directions of the H-and J-bands resulting from herringbone arrangement. To this end, we shall provide a detailed analysis and further quantitative interpretation of the polarization dependence of absorption which will lead to verification of the internal molecular packing and the dynamical processes discussed above.

3.3. Herringbone model

Fig. 4 illustrates the herringbone model in which each chain is a one-dimensional J-aggregate of N molecules. Each molecule is assumed to have a dipole-allowed transition between the ground

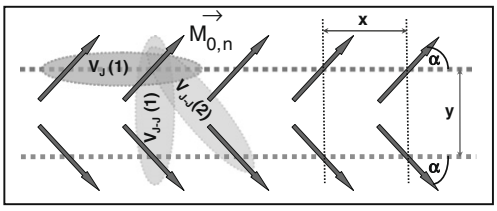

Fig. 4. The herringbone model and the leading intra- and interchain interactions.

state and the excited state of interest, specified by the excitation energy E_n and the transition dipole moment $\vec{M}_{0,n}$.

In the absence of disorder the excitation energies are equal to E_0 for all n. The dipoles are aligned equidistant (x) and are parallel to each other along the aggregate axis, $\vec{M}_{0,n} = M_0\hat{M}_{0,n}$ M_0 equal for all n). α and y define, respectively, the orientation of dipoles relative to the aggregate axis and the interchain separation. V_J and V_{J-J} stand, respectively, for the intrachain and the interchain dipolar interactions.

For infinitely long homogeneous aggregates and by including only the leading interactions indicated in Fig. 4, the peak positions are on the red/at the bottom of both bands for $V_J(1) < 0$, $V_{J-J}(1) > 0$, and $V_{J-J}(2) < 0$ and are located at [31]

$$E_J(\max) = E_0 + 2V_J(1) - [V_{J-J}(1) + 2V_{J-J}(2)] \quad (2a)$$

$$E_H(\max) = E_0 + 2V_J(1) + [V_{J-J}(1) + 2V_{J-J}(2)] \quad (2b)$$

where, $V_J(1)$, $V_{J-J}(1)$ and $V_{J-J}(2)$ can be expressed by Eq. (A3) in the Appendix.

In the point dipole approximation the positions of the absorption peaks with respect to the monomeric transition energy and their relative strength are determined by M_0^2/x^3 and M_0^2/y^3, and α (see Eq. (A3)). With these three independent parameters the model assures the versatility of tuning the asymmetry in the peak positions and of adjusting the relative strengths of the H- and J-/Davydov split bands.

The transition dipole moments corresponding to the H- and the J-peaks are polarized, respectively, along the aggregate axis and perpendicular to it and have the isotropic absorbance ratio of $f(\alpha) = A_{iso,H}/A_{iso,J} = \cot g^2\alpha$. For finite inhomogeneous aggregates a redistribution of the peak intensities into a band of transitions and some intensity borrowing between the two bands will be exhibited. The average polarization direction of the H- and the J-bands will no longer be exactly parallel and perpendicular to the aggregate axis.

3.4. Simulation of the isotropic absorption spectrum

The isotropic absorption spectrum, A_{iso}, has been simulated on the basis of Frenkel exciton formalism in the point dipole approximation [26,27]. The band shapes/widths were modeled by including diagonal energetic disorder (Gaussian inhomogeneous broadening) and exciton–phonon coupling (Lorentzian lifetime broadening). The inhomogeneous broadening was implemented by using the method of Fidder et al. [28] and the exciton relaxation was considered in the limit of weak, on-site exciton–phonon coupling [29]. A summary of the formalism and the details of its numerical implementation were provided in the Appendix.

A set of A_{iso} simulations with the peaks matching the experimental data, i.e., at 505 nm (the H-peak) and 594 nm (the J-peak) are given in Fig. 5a. Fig. 5b shows the resolution of the H- and J-band shapes at a specific value of α ($\alpha = 27°$). Fig. 5c shows the effects of the variations of the interchain distance on A_{iso}. The dynamical parameters of the simulations given in Fig. 5 are adapted from our previous simulations of A_{iso} in ionic solution [16].

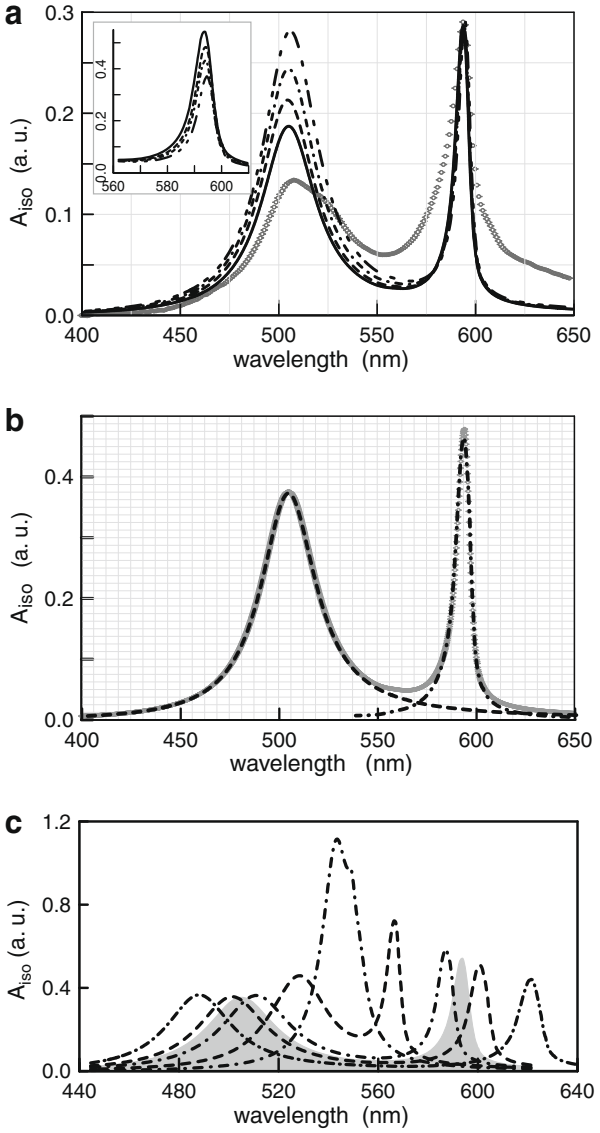

Fig. 5. Several simulations of A_{iso} with the H- and J-band peak positions satisfying the experimental data (panel a). The resolution of the H- and J-band shapes using the A_{iso} simulation satisfying the experimentally observed peak positions at $\alpha = 27°$ (panel b). Effects of variations of the interchain distance on A_{iso} (panel c). Please refer to the text and the Appendix for the definitions of the simulation parameters. In panel a, the symbols stand for the experimental data at $\theta = 80°$. In panel a and in its insert the simulations are respectively scaled to the J-peak and the H-peak intensity of the experiment. In all simulations $N = 50$, the averaging is over 10^3 cycles, and the dynamical parameters are $\sigma = 200\ cm^{-1}$, $\hbar S_{intra} = 500\ cm^{-1}$ and $\hbar S_{inter} = 2500\ cm^{-1}$. The structural parameter sets for panel a, in the order {α (°), M_0^2/x^3 (debye^2/nm^3), M_0^2/y^3 (debye^2/nm^3)}, are {24, 62.44, 355.86}, dash-dot-dot, {26, 64.48, 347.3}, dash-dot, {28, 67.97, 341.81}, dash, and {30, 73.12, 329.53}, solid. In panel b, A_{iso} (gray solid), $A_{iso,H}$ (dash) and $A_{iso,J}$ (dash-dot) and $\alpha = 27°$, $M_0^2/x^3 = 66.62$ debye^2/nm^3 and $M_0^2/y^3 = 343.91$ debye^2/nm^3. In panel c, the solid line spectrum satisfies the experimental peak positions. The simulation parameters, $M_0 = 10$ debye, $x = 1.11$ nm, $\alpha = 30°$ and $y = 0.600$ nm, 0.650 nm, 0.672 nm, 0.700 nm, 0.850 nm and 1.500 nm (from left to right).

For finite inhomogeneous aggregates the leading interactions, $V_J(1)$, $V_{J-J}(1)$, and $V_{J-J}(2)$, are still the most important factors determining the peak positions of the H- and J-bands (see Eqs. (2a) and (2b)). While disorder and dynamical processes basically account for the band shapes/widths and together with the longer range interactions ensue further adjustment of the peak positions. The relative strengths of the H- and J-bands are basically determined by α. The band shapes remain intact for a given set of dynamical parameters.

The variation of interchain distance is probably the main reason for the spectral heterogeneity observed in the data of Fig. 2 (discussed in more detail in [16]). The spectra simulated in Fig. 5c show that the asymmetry of the band peaks around the monomeric transition and the band gap width are basically tuned by the interchain couplings. As the two straps get loosely coupled some red (blue) shift is experienced by the H- (J-) band and the band gap gets narrower. Eventually, the Davydov split bands merge into a single exciton band in the gap, which in the infinite homogenous limit is a single state positioned at $E_0 + 2V_J(1)$. The widths of the Davydov split bands become narrower as they merge in the gap. Conversely, as the interchain coupling gets stronger the band gap gets wider and the satellite bands are formed on respectively the blue and the red tails of the reference H- and J-peaks.

3.5. Further comments on polarized absorption

Eq. (1a) can be adapted to analyze the experimental data described above. The polarization direction dependence of the relative changes in the absorbance of each band can be evaluated by considering

$$R_H(\theta) = \frac{A_{II,H}|_\theta}{A_{II,H}|_{\theta_{ref}}} = \frac{1 + 2P_2(\cos(\theta - \gamma)) \cdot \langle P_2(\cos\beta_v)\rangle_H}{1 + 2P_2(\cos(\theta_{ref} - \gamma) \cdot \langle P_2(\cos\beta_v)\rangle_H} \quad (3a)$$

and

$$R_J(\theta) = \frac{A_{II,J}|_{\theta_{ref}}}{A_{II,J}|_\theta} = \frac{1 + 2P_2(\cos(\theta_{ref} - \gamma)) \cdot \langle P_2(\cos\beta_v)\rangle_J}{1 + 2P_2(\cos(\theta - \gamma) \cdot \langle P_2(\cos\beta_v)\rangle_J} \quad (3b)$$

where θ_{ref} can be any one of the experimentally controlled θ values. The terms involving $P_2(\cos\beta_v)$ are weighted averages over different excitonic states contributing to the absorption over the H- and J-bands.

In addition the polarization dependence of relative absorbance of the two bands can be evaluated by considering

$$R_{H/J}(\theta) = \frac{A_{II,H}|_\theta}{A_{II,J}|_\theta} = f(\alpha)\frac{1 + 2P_2(\cos(\theta - \gamma)) \cdot \langle P_2(\cos\beta_v)\rangle_H}{1 + 2P_2(\cos(\theta - \gamma)) \cdot \langle P_2(\cos\beta_v)\rangle_J} \quad (4)$$

where $f(\alpha) = A_{iso,H}/A_{iso,J}$.

To utilize Eqs. (3) and (4) it is necessary to obtain reliable estimates of $A_{II,H}|\theta$ and $A_{II,J}|\theta$ out of the experimental spectra. Then, the behaviors of $R_J(\theta)$, $R_H(\theta)$ and $R_{H/J}(\theta)$ can be displayed as a function θ. Simultaneous fits of these three data sets yield the orientation of the aggregate axis with respect to the macroscopic alignment axis, γ, the average polarization of the H- and J-bands, $\langle P_2(\cos\beta_v)\rangle_H$ and $\langle P_2(\cos\beta_v)\rangle_J$, and $f(\alpha)$ (or α). Once α is determined further structural quantification, i.e., the values of M_0^2/x^3 and M_0^2/y^3 can be obtained through Eqs. (2) and (A3).

3.6. Analysis of the experimental data

In the presence of spectral heterogeneity observed we have not attempted fitting the absorption spectra of Fig. 2. Instead a specific herringbone packing has been assumed to represent majority of the aggregates and thus to account for the absorption of the H- and J-bands around the band maxima to a large extent. The polarization direction dependences of the H- and J-band absorption strengths have been followed through the changes in the overall intensities of these two major bands. By following the overall intensity the polarization dependence of a multitude of individual excitonic transitions making up the H- and J-bands is ignored. Owing to the superradiant state nature of the J-/H-bands the majority of the transitions under each band are expected to have similar individual excitonic transition dipole moment directions. Therefore, this approach can be considered as a reasonable first order approximation.

The H- and J-band shapes that have been resolved in Fig. 5b are employed in the analysis. The positions and widths of the H- and J-bands and of the monomeric band are expected to be independent of polarization. In addition the H- and the J-band absorption are expected to vary independently as a function of the polarization direction. The intensity of the monomeric band has been determined by employing the TTBC absorption spectrum in methanol and by co-adjusting the intensity of the H-band to fit the blue part of the $\theta = 80°$ experimental spectrum that has the largest relative monomeric contribution. This monomeric contribution of fixed intensity and the H- and J-band shapes whose intensities have

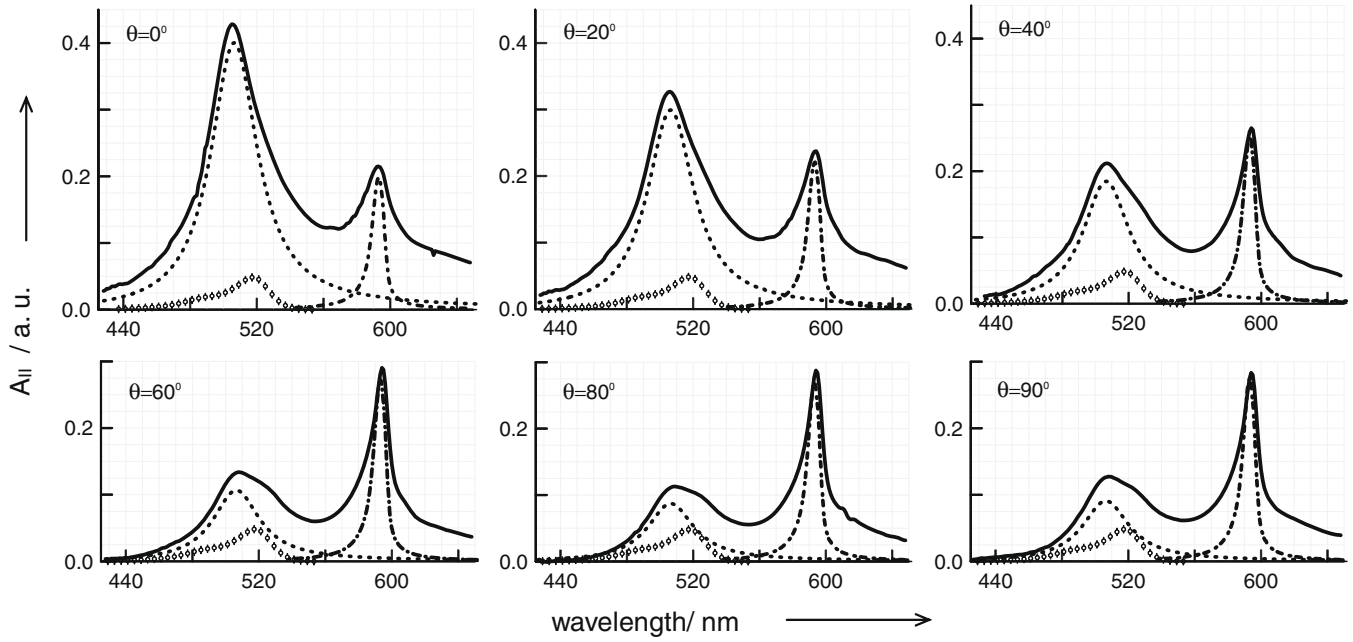

Fig. 6. "Decomposition" of the experimental absorption spectra at $\theta = 0°$, 20°, 40°, 60°, 80°, and 90° using the H- (short dash) and J-band (dash-dot) shapes resolved in Fig. 5b, and the monomeric contribution (symbols) whose intensity is adjusted as discussed in the text. The areas under the H- and J-band shapes were taken as the experimental values of $A_{II,H}|\theta$ and $A_{II,J}|\theta$.

been adjusted independently at each polarization were then employed for all polarization directions between $\theta = 0°$ and 180°. Fig. 6 shows the resolution of the experimental spectra for polarizations with $\theta \leqslant 90°$. The polarized absorption spectra for $90° < \theta \leqslant 180°$ were resolved similarly (the results are not shown for brevity). The absorbance of the H- and J-band shapes at each polarization were taken as the experimental values of $A_{II,H}|\theta$ and $A_{II,J}|\theta$ and have been used to evaluate $R_J(\theta)$, $R_H(\theta)$ and $R_{H/J}(\theta)$. θ_{ref} was taken to be 80°.

The polarization direction dependences of, $R_H(\theta)$, $R_J(\theta)$ and $R_{H/J}(\theta)$ have been displayed respectively in panels a, b, and c of Fig. 7. Also given in each panel of Fig. 7 are the fits obtained via Eqs. (3) and (4). The fits to $R_H(\theta)$ and $R_J(\theta)$ have yielded γ values between −12 and −14, $\langle P_2(\cos\beta_\nu)\rangle_H$ values between 0.567 and 0.602, and $\langle P_2(\cos\beta_\nu)\rangle_J$ values between −0.102 and −0.136. The latter values would translate to "β_H" = 31°–32.5° and "β_H" = 59–60.5 for a single band edge state. Even in the presence of disorder the superradiant state characters of the J- and H-band edges are manifested. It can, therefore, be reasoned that the average polarization of the band edge states are less than 30° (the H-band) and more than 60° (the J-band), i.e., the polarizations of H-band edge transitions are still close to being parallel to the aggregate axis and the polarizations of J-band edge transitions are close to being perpendicular to the aggregate axis. The polarization dependence of $R_{H/J}(\theta)$ was then assessed via Eq. (4) and $f(\alpha)$ was found to be 3 upon fitting the absolute scale of $R_{H/J}(\theta)$ versus θ data. $f(\alpha) = 3$ corresponds to $\alpha = 30°$ if evaluated in the infinite homogeneous aggregate limit. More accurately, $\alpha = 27°$ (i.e., the simulation given in Fig. 5b) was found to satisfy $f(\alpha) = 3$ for inhomogeneous aggregates considered in this study. For $\alpha = 27°$ Eqs. (2) and (A3) give the values of $M_0^2/x^3 = 66.62$ debye$^2/nm^3$ and $M_0^2/y^3 = 343.91$ debye$^2/nm^3$. The internal molecular packing predicted is very similar to the one proposed for TTBC in ionic aqueous solution for which the simulation has been shown in Fig. 3. Table 1 compares the structural parameters of the two samples in the range of M_0 values reported for several other cyanines [12–14].

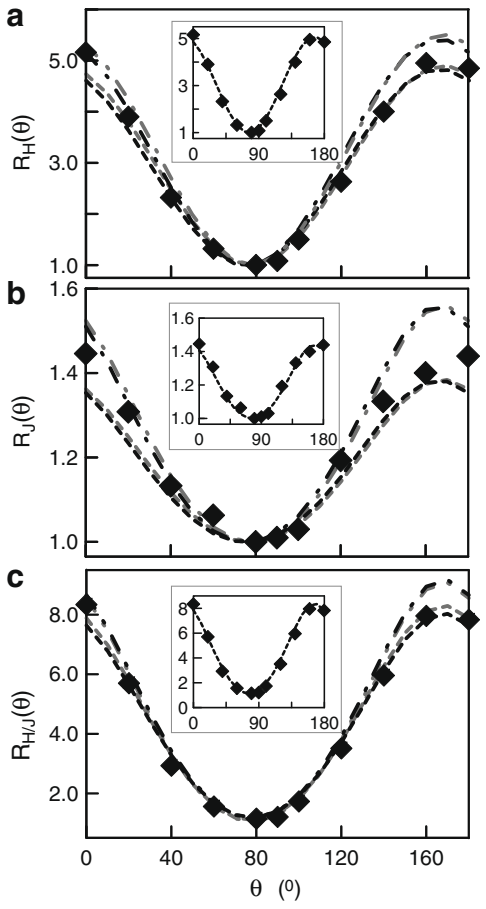

Fig. 7. The fits to $R_H(\theta)$, $R_J(\theta)$ and $R_{H/J}(\theta)$ versus θ. The symbols indicate the data points extracted as discussed in relation to Fig. 6. Panel a, $\langle P_2(\cos\beta_\nu)\rangle_H = 0.567$ (dash-dot) and $\langle P_2(\cos\beta_\nu)\rangle_H = 0.602$ (dash), $\gamma = -12°$ (gray) and $\gamma = -14°$ (black). The insert of a, $\langle P_2(\cos\beta_\nu)\rangle_H = 0.579$ and $\gamma = -13°$. Panel b, $\langle P_2(\cos\beta_\nu)\rangle_J = -0.102$ (dash) and $\langle P_2(\cos\beta_\nu)\rangle_J = -0.136$ (dash-dot), $\gamma = -12°$ (gray) and $\gamma = -14°$ (black). The insert of b, $\langle P_2(\cos\beta_\nu)\rangle_J = -0.114$ and $\gamma = -13°$. Panel c, $\gamma = -12°$ and $\langle P_2(\cos\beta_\nu)\rangle_H$, $\langle P_2(\cos\beta_\nu)\rangle_J$ pairs are, {0.567, −0.102}, dash, black, {0.602, −0.102}, dash, gray, {0.567, −0.136}, dash-dot, black, {0.602, −0.136}, dash-dot, gray. The insert of c, $\langle P_2(\cos\beta_\nu)\rangle_J = -0.114$, $\langle P_2(\cos\beta_\nu)\rangle_H = 0.579$ and $\gamma = -13°$.

Table 1
The structural parameters and the leading interaction strengths for the simulations.

System studied	M_0 = 8 debye α (°) x (nm) y (nm)	M_0 = 12 debye α (°) x (nm) y (nm)	V_J (1) (cm^{-1})	V_{J-J} (1) (cm^{-1})	V_{J-J} (2) (cm^{-1})
TTBC in PVA thin films	27 0.99 0.57	27 1.29 0.75	−464	2090	−227
0.2 mM TTBC in 0.01 M NaOH solution (Ref. [16])	27 1.03 0.57	27 1.35 0.75	−406	2062	−213

4. Concluding remarks

The structure–spectroscopy–function relationship of the TTBC aggregates dispersed in PVA thin films was investigated using measurements and simulations of polarized absorption spectra.

Macroscopically well-defined alignment axis offered by vertical spin coating allowed a very convenient control for the systematic measurements of the incident polarization dependence of the spectral response of the system. System-specific modeling approach that we have adopted is essential since depending on the particular preparation method different aggregate morphologies can be exhibited for a given cyanine molecule [16,32].

Due to heterogeneity of the samples further refinement of the line shapes/dynamics has not been possible. Thus the inclusion of dynamical processes in the modeling has not yielded as essential as it has been in the absence of heterogeneities [16]. The dynamical aspects of the model could be further tested by investigating the temperature-dependence of the line shapes and/or by observing the dynamics in the time-domain (see e.g., Refs. [15,17–20]).

Nevertheless, the general suggestions on the structure, excited states and relaxation dynamics discussed above are expected to hold for other cyanine aggregates which show the same generic features [32–34].

Acknowledgements

S.Ö. acknowledges TÜBİTAK–NSF joint grant TBAG U-12. We thank to John R. Lombardi for his support.

Appendix A

A.1. Theoretical

The Frenkel exciton Hamiltonian of an aggregate of N molecules is [26,27]

$$H_{ex} = \sum_{n=1}^{N} E_n |n\rangle\langle n| + \sum_{n,m} V(n,m)|n\rangle\langle m| \tag{A1}$$

In (A1), $|n\rangle$ is the state, in which the nth molecule of the aggregate is excited while all the others are in the ground state, E_n is the excitation energy of the nth molecule (site energy) and $V(n,m)$ denotes the intermolecular interactions.

The diagonalization of H_{ex} gives the excitonic spectrum of the aggregate with the eigenstates $|v\rangle$ and the eigenenergies E_v, for $v = 1,\ldots, N$,

$$|v\rangle = \sum_{n=1}^{N} C_{vn}|n\rangle \tag{A2a}$$

$$E_v C_{vn} = \sum_{m=1}^{N} \langle n|\mathrm{H}|m\rangle C_{vm} \tag{A2b}$$

In the case of dipolar interaction in the point dipole approximation

$$V(n,m) = 5.04 \frac{M_{0,n} M_{0,m} \kappa_{nm}}{r_{nm}^3} \ \mathrm{cm}^{-1} \tag{A3}$$

where $M_{0,n}$, the dipole moment strength, is in debye and $r_{nm} = \vec{r}_{nm}/\hat{r}_{nm}$, the center to center distance from the nth molecule to the mth molecule, is in nm. κ_{nm} is given by

$$\kappa_{nm} = \hat{M}_{0,n} \cdot \hat{M}_{0,m} - 3(\hat{M}_{0,n} \cdot \hat{r}_{nm})(\hat{M}_{0,m} \cdot \hat{r}_{nm}) \tag{A4}$$

The isotropic absorption strength of the vth excitonic transition is

$$A_{\mathrm{iso},v} = \vec{M}_v \cdot \vec{M}_v \tag{A5}$$

with

$$\vec{M}_v = \sum_{n=1}^{N} C_{vn} \vec{M}_{0,n} \tag{A6}$$

The (isotropic) absorption spectrum can be expressed as

$$A_{\mathrm{iso}}(E) = \left\langle \left(\sum_{v=1}^{N} \Lambda_v (E - E_v) \right) \right\rangle \tag{A7}$$

where $\Lambda_v(E - E_v)$ represents a Lorentzian centered at E_v with a fwhm of Γ_v (the decay rate of the state $|v\rangle$). The area under $\Lambda_v(E - E_v)$ is equal to $A_{\mathrm{iso},v}$. The brackets indicate averaging over an ensemble of a large number of aggregates, each of N molecules with a randomly generated set of uncorrelated site energies.

The width of each Lorentzian (Γ_v) is attributed to broadening by phonon-assisted relaxation. The static disorder leads to (weak) localization of the exciton states [28]. The coupling of the weakly localized excitons to the molecular vibrations and/or to the vibrations of the host medium, cause scattering between different exciton states. The generic expression for the transition rate from the exciton state $|v\rangle$ to the exciton state $|\mu\rangle$ in the limit of weak, linear, on-site exciton–phonon coupling is [29]

$$W_{\mu v} = \sum_{n=1}^{N} S(|E_v - E_\mu|) C_{\mu n}^2 C_{vn}^2 x \begin{cases} \langle n_{\mathrm{phonon}}(E_\mu - E_v)\rangle, & E_v < E_\mu \\ 1 + \langle n_{\mathrm{phonon}}(E_v - E_\mu)\rangle, & E_v > E_\mu \end{cases}. \tag{A8}$$

The transition rate is expressed in terms of the overlap integral of excitation probabilities for the states $|v\rangle$ and $|\mu\rangle$. The spectral function $S(|_v\text{-}E_\mu|)$ contains the dependencies of the exciton–phonon coupling strength and of the phonon density of states on energy. The upper (the lower) expression stands for absorption (emission) of a phonon on site n. $\langle n_{\mathrm{phonon}}(E_{\mathrm{phonon}})\rangle$ is the mean occupation number of a phonon state with energy E_{phonon} at temperature T and is taken as the Bose distribution

$$\langle n_{\mathrm{phonon}}(E_{\mathrm{phonon}})\rangle = [\exp(\beta \cdot E_{phonon}) - 1]^{-1} \tag{A9}$$

with $\beta = (k_B T)^{-1}$ and $k\beta$, the Boltzmann constant. The transition rates obey the principle of detailed balance, $W_{\mu v} = W_{v\mu}[\exp(\beta \cdot (E_v\text{-}E_\mu)]$, and the equilibrium (in the absence of radiative decay) is characterized by the Boltzmann distribution.

The fwhm of the Lorentzian corresponding to the exciton state $|v\rangle$ is defined as

$$\Gamma_v = \sum_{\mu \neq v} \hbar W_{\mu v} \tag{A10}$$

A.2. Numerical

The Hamiltonian, H_{ex} (A1) is constructed in the point dipole approximation by including all intermolecular interactions in each J-aggregate chain (V_J) and between the two chains (V_{J-J}). The angular variable α and the factors M_0^2/x^3 and M_0^2/y^3 which scale the intra- and interchain interactions are treated as fit parameters. The eigenfunctions (A2a) and the eigenenergies (A2b) are obtained by numerically diagonalizing H_{ex} for a particular realization of site energies on the diagonal. The site energies are assumed to be uncorrelated random variables, each with a Gaussian distribution function centered at the monomeric energy (514 nm) and of the same fwhm (σ). σ has been an empirical fit parameter. The inhomogeneous broadening is implemented by assigning the site energies out of these distributions at each cycle of random number generation and a total of 10^3 cycles are considered. During each realization of disorder the transition rates (A8) are calculated at room temperature. The spectral function $S(|E_v - E_\mu|)$ which, scales the transition rate between the exciton states $|v\rangle$ and $|\mu\rangle$ is treated as an empirical fit parameter. Two different spectral functions are considered; one for the transitions from the H-band to the J-band, $S_{\mathrm{inter}}(E)$ and one for the transitions within each band, $S_{\mathrm{intra}}(E)$. Moreover, $S_{\mathrm{intra}}(E)$ and $S_{\mathrm{inter}}(E)$ are assumed to be constant for all transitions in the respective spectral regimes. The widths calculated by A10 are used to execute the Lorentzian broadening described by A7. The Lorentzian dressing is performed with a spectral digitization of 2.0 cm^{-1}.

References

[1] E.E. Jelley, Nature 138 (1936) 1009.
[2] G. Scheibe, Angew. Chem. 50 (1937) 51.
[3] T. Kobayashi (Ed.), J-Aggregates, World Scientific Publication, Singapore, 1996.
[4] H. Herz, Photo. Sci. Eng. 18 (1974) 323.
[5] R.P. Haugland, in: J. Gregory (Ed.), Handbook of Fluorescent Probes and Research Products, Molecular Probes, Eugene, OR, USA, 2002, p. 871.
[6] R.M. Jones, L. Lu, R. Helgeson, T.S. Bergstedt, D.W. McBranch, D.G. Whitten, Proc. Natl. Acad. Sci. USA 98 (2001) 14769.
[7] H. Van Amerongen, R. Van Grondelle, L. Valkunas, Photosynthetic Excitons, World Scientific, Singapore, 2000.
[8] L.A. Bumm, J.J. Arnold, M.T. Cygan, T.D. Dunbar, T.P. Burgin, L. Jones, D.L. Allara, J.M. Tour, P.S. Weiss, Science 271 (1996) 1705.
[9] M. Furuki, O. Wada, L.S. Pu, Y. Sato, H. Kawashima, T. Tani, J. Phys. Chem. B 103 (1999) 7607.
[10] K. Misawa, H. Ono, K. Minoshima, T. Kobayashi, Appl. Phys. Lett. 63 (1993) 577.
[11] K. Misawa, S. Machida, K. Horie, T. Kobayashi, Chem. Phys. Lett. 240 (1995) 210.
[12] C. Didraga, A. Pugzlys, R.P. Hania, H. von Berlepsch, K. Duppen, J. Knoester, J. Phys. Chem. B 108 (2004) 14976. and the references therein.
[13] K.J. Ikegami, Chem. Phys. 121 (2004) 2337.
[14] D.M. Basko, A.N. Lobanov, A.V. Pimenov, A.G. Vitukhnovsky, Chem. Phys. Lett. 369 (2003) 192.
[15] M. Bednarz, V.A. Malyshev, J. Knoester, J. Chem. Phys. 120 (2004) 3827.
[16] B. Birkan, D. Gülen, S. Özçelik, J. Phys. Chem. B 110 (2006) 10805.
[17] D.J. Heijs, V.A. Malyshev, J. Knoester, J. Chem. Phys. 123 (2005) 144507.
[18] M. Bednarz, V.A. Malyshev, J. Knoester, Phys. Rev. Lett. 91 (2003) 217401.
[19] D.J. Heijs, V.A. Malyshev, J. Knoester, Phys. Rev. Lett. 95 (2005) 177402.
[20] A. Pugzlys, R. Augulis, P.H.M. van Loosdrecht, C. Didraga, V.A. Malyshev, J. Knoester, J. Phys. Chem. B 110 (2006) 20268.
[21] F.J.M. Hoeben, P. Jonkheijm, E.W. Meijer, A.P.H.J. Schenning, Chem. Rev. 105 (2005) 1491.
[22] C.C. Gradinaru, S. Özdemir, D. Gülen, I.H. van Stokkum, R. van Grondelle, H. van Amerongen, Biophys. J. 75 (1998) 3064.
[23] V. Sundström, T. Pullerits, R. van Grondelle, J. Phys. Chem. B 103 (1999) 2327.

[24] H.M. Cho, M. Vaswani, T. Brixner, J. Stenger, G.R. Fleming, J. Phys. Chem. B 109 (2005) 10542.
[25] R. Van Grondelle, V.I. Novoderezhkin, Phys. Chem. Chem. Phys. 8 (2006) 793.
[26] R.S. Knox, Theory of Excitons, Academic Press, New York, 1963.
[27] A.S. Davydov, Theory of Molecular Excitons, Plenum, New York, 1970.
[28] H. Fidder, J. Knoester, D.A. Wiersma, J. Chem. Phys. 95 (1991) 7880.
[29] J.A. Leegwater, J.A. Durrant, D.A. Klug, J. Phys. Chem. B 101 (1997) 7205.
[30] L. Monnerie, in: I.M. Ward (Ed.), Structure and Properties of Oriented Polymers, Wiley, New York, 1975, p. 199.
[31] G. Juzeliūnas, J. Knoester, J. Chem. Phys. 112 (2000) 2325.
[32] H. von Berlepsch, S. Kirstein, C. Böttcher, J. Phys. Chem. B 108 (2004) 18725.
[33] I.G. Scheblykin, O.Y. Sliusarenko, L.S. Lepnev, A.G. Vitukhnovsky, M. Van der Auweraer, J. Phys. Chem. B 105 (2001) 4646.
[34] I.O. Shklyarevskiy, P.C.M. Christianen, E. Aret, H. Meekes, E. Vlieg, G. Deroover, P. Callant, L. van Meervelt, J.C. Maan, J. Phys. Chem. B 109 (2005) 16386.